Microstructural effects on properties of as-fabricated Inconel 625 with direct energy deposition process

Theo-Neal Booysen[1]*, *Tamba* Jamiru[2], *Taoreed* Adegbola[3] & *Nana* Arthur[4]

[1] Department of Mechanical and Mechatronics, Tshwane University of Technology, South Africa, Staatsartillerie Road, Pretoria West, Pretoria, 0183

[2] Department of Mechanical and Mechatronics, Tshwane University of Technology, South Africa, Staatsartillerie Road, Pretoria West, Pretoria, 0183

[3] Department of Mechanical and Mechatronics, Tshwane University of Technology, South Africa, Staatsartillerie Road, Pretoria West, Pretoria, 0183

[4] CSIR, Photonics Centre, Laser Enabled Manufacturing Group, Pretoria Campus, 0001, South Africa

Graphical abstract

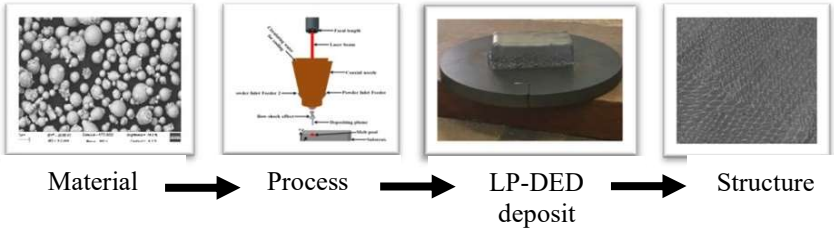

Abstract. Three-dimensional printing (3D), also known as metal additive manufacturing (MAM), fabricates parts or components from different feedstocks: wires, powders or sheets. This process differs from traditional manufacturing techniques such as casting, moulding, or subtracting existing materials. In the development and improvement or fabrication of new materials for higher strength and various applications, the type or character of a material is very important as this will ascertain the strength of the finished product. Direct energy technology can be used to fabricate and repair parts or components with the following two fabrication methods: laser wire-directed energy deposition (LW-DED) or laser powder-directed energy deposition (LP-DED). In this research, laser powder-directed energy deposition (LP-DED), a MAM process method, was employed to fabricate Inconel 625. The LP-DED process uses a laser as a heat source and rapidly

* Corresponding author: twjbooysen@gmail.com

melts metallic powders of different chemical compositions to fabricate complex structures, which is an innovative three-dimensional material processing technology. The as-fabricated (AF) sample specimens were investigated to determine the microstructural development, microhardness and sample defects. The microstructural features were analysed using two experimental surface microscopy methods: light optical microscopy (LOM) and scanning electron microscopy (SEM). The morphological grain structure within the samples was predominantly cellular, columnar and columnar-dendritic. Energy dispersive X-ray (EDX) and X-ray diffraction (XRD) analysis were performed to determine the chemical composition and crystallographic structures of virgin gas atomisation (GA) powder and as-fabricated sample. The XRD peaks in samples composed of face-centred-cubic (FCC) γ-nickel phase. The material microhardness was studied by performing Rockwell hardness test (HRB) with a fluctuated trend averaging 98.9 – 101.6 HRB. The relationship between processing, microstructure, grain structure and material hardness was systematically summarised and established. The study concluded with research suggestions on LP-DED of Inconel 625.

1 Introduction

Metal additive manufacturing (MAM) has revolutionised the metal manufacturing industry as it allows the fabrication of complex near net three-dimensional (3D) metal components or parts with both minimal retooling during the fabrication process and post-processing compared with traditional methods (cast and wrought) [1]. Understanding process development and the prediction of microstructure and mechanical properties of MAM materials is fundamental. Machine and computational learning techniques in MAM have proven to be exceptionally useful tools for accumulating insight into MAM processes and conditions [1]. However, the MAM process has challenges, including thermo energy and the molten process of metallic powders or wire during melting and resolidification. The thermal aspect during heat transfer subsequently affects the solid and solid-to-solid phase transformation and macroscale of any change in temperature [2, 3]. The information from microscale models will predict important characteristics of the material microstructure, including grain morphology, grain size, aspect ratio, precipitate volume fraction, and size and build-up of plastic strain [1-3]. This process must be developed to translate these microstructural characteristics into mechanical property predictions [1-2]. The focus has been on process parameters to understand MAM materials and not so much on the mechanical response of MAM.

In this study, MAM techniques for producing metal components from metal powders with a focus on microstructure science of metals and mechanical properties, heat transfer, solidification and post-processing metallurgy are compared and analysed. The metallurgical component manufactured using additive manufacturing is determined with a chemical reaction at a certain temperature experienced by the material. Heat transfer has different applications for powder bed fusion (PBF), direct energy deposition (DED), and additive manufacturing, and the metallurgical principle for both processes yields similar outcome [2].

Materials are subjected to some kind of loading, and their prediction to produce reliable designs must be correct and the properties with their numerous metallurgical variables have to be understood [2]. A combination of metals has been produced for commercial production using additive manufacturing, but recent efforts have made it possible for the continuous development of new materials suitable for MAM processes [2, 4]. This paper focuses mainly on as-fabricated (AF) laser powder-directed energy deposition (LP-DED) Inconel 625

samples and the relationship between processing, microstructure, grain structure, and material hardness [2].

1.1 Why Inconel 625?

Inconel is group of superalloys. Particularly, Inconel 625 is one of the most recognised nickel-based superalloys and is ideal for high-temperature applications. The key factor of nickel-based alloy strength can be explained by precipitation hardening, which is the most useful process at high temperatures [2]. Inconel 625 is a type of solid solution-strengthened nickel-based super alloy, with molybdenum and niobium in a nickel chromium matrix [2-5]. Inconel 625 is resistant to wear, corrosion and fatigue, and further displays good weldability. Table 1 lists the chemical element composition ranges of Inconel 625.

Table 1. Element composition with percentage ranges and limits of Inconel 625 (wt%)[2,7].

Nickel (58% min)	Chromium (20–23%)	Iron (5% max)
Molybdenum (8–10%)	Copper (0.5% max)	Aluminium (0.4% max)
Niobium (3.2–4.1%)	Silicon (0.5% max)	Carbon (0.10% max)
Sulphur (0.015% max)	Manganese (0.5% max)	Phosphorus (0.02% max)
Titanium (0.4% max)		

This superalloy is currently used in aviation gas turbines, the chemical and medical industries, petrochemical equipment, rocket engines, nuclear reactors, submarines and other applications that operate at high temperatures with chemical resistance [2]. MAM of Inconel 625 is appropriate for developing custom or complex parts for the aerospace, marine and possibly biomedical fields [2]. The shape of most Inconel 625 components is complex and expensive to manufacture using traditional methods due to extensive machining. The microstructure of MAM nickel-based superalloys Inconel 625 is dependent on specific processes with different applications, such as process parameters and deposited geometry [2, 8]. When compared with traditional and wrought fabrication methods, solidification in the MAM process occurs more rapidly as the finer grain size is modified to suit a particular grain structure [2]. LP-DED uses a laser as feedstock to heat and melt the metallic powder, which solidifies rapidly. It is a rapid fabrication method for fabricating high-quality metallic 3D parts or components. This fabrication is possible without the aid of any tools that require retooling during fabrication processing. MAM is a remarkably innovative process that opens up opportunities for companies to improve their manufacturing efficiency. The technology allows design freedom with minimum constraints compared with traditional manufacturing methods.

1.2 Materials and processing

The Inconel 625 metallic powder was supplied by Carpenter Additive, a business unit of Carpenter Technology Corporation. The gas-atomisation (GA) powder particles have a particle size distribution of between 20 μm and 50 μm with almost spherical shapes as observed with scanning electron microscopy (SEM). Figure 1a illustrates the use of Inconel 625 as a feedstock material. The Inconel 625 sample specimen was fabricated using an Optomec application workstation, an LP-DED system with motion numerical control with a

five-axis operation option, a coaxial metallic powder feeder, and an automatic feeding device as illustrated in Figure 1b. Figure 1c illustrates the fabricated sample specimen with dimensions 40 mm × 20 mm × 10 mm. Table 2 lists the fabrication process parameters.

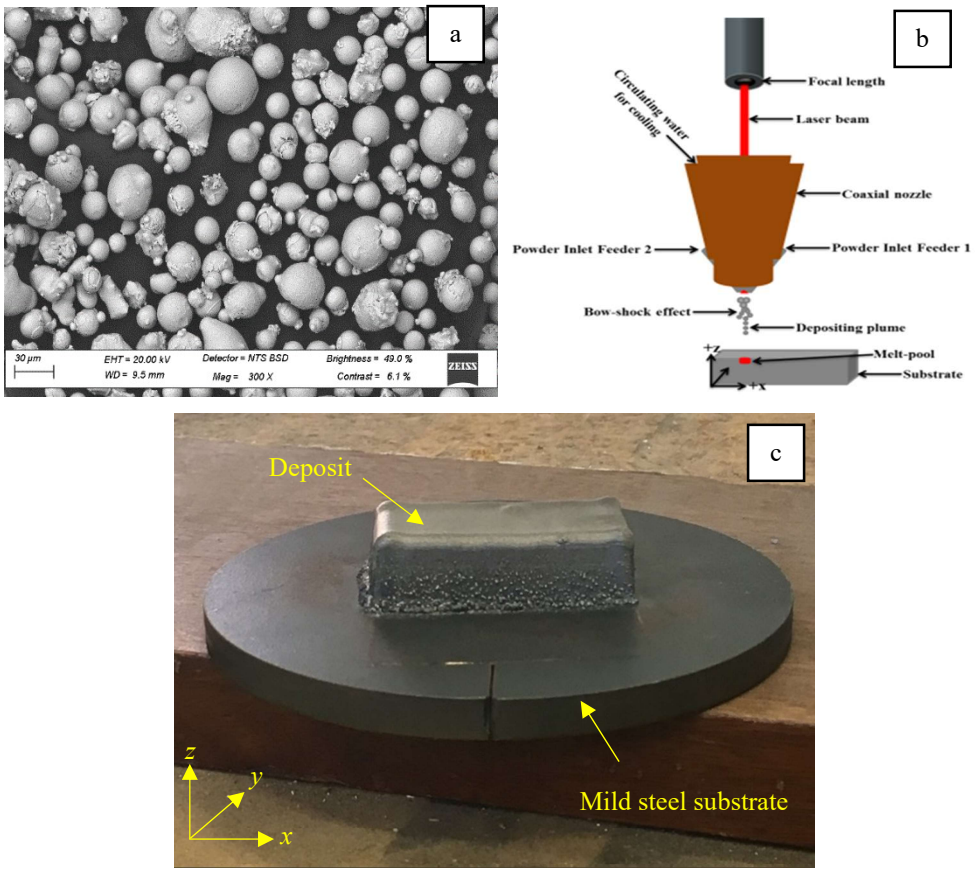

Fig. 1.a) GA metallic Inconel 625 powder particles; **b)** LP-DED process (courtesy [10]); and **c)** AF Inconel 625 on substrate.

Table 2: Fabrication process parameters.

Laser power	Laser type	Laser scanning speed	Powder feed rate	Layer thickness	Operation atmosphere argon approx.	Scanning pattern
400 W	IPG fibre laser	10.58 mm/s	5.23 g/min	20 µm	50–100 ppm	Bidirectional

1.3 Sample preparation

The AF Inconel 625 sample specimens were wire-cut from the mild steel substrate and embedded in Bakelite hot mounting powder resin using a thermal-compression mounting machine [2]. A standard thermal moulding process was applied as illustrated in Figure 2. Thereafter, the specimens were ground and polished in line with standard procedure. The

samples were immersed in freshly mixed acid – 15 ml hydrochloric acid (HCI), 10 ml acetic acid (CH_3COOH), and 10 ml nitric acid (HNO_3) – for ±35 seconds [2, 5]. Ethanol was used to clean the surface, whereafter the samples were dried using hot air ready for light optical microscopy (LOM) and SEM microstructure analysis.

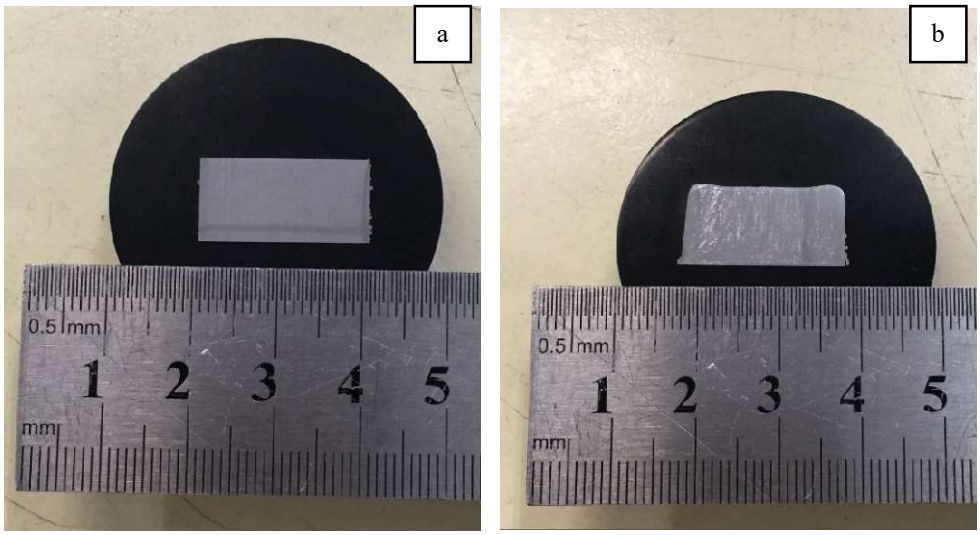

Fig. 2. AF Inconel 625 samples: **a)** parallel and **b)** perpendicular to the building direction.

1.4 Microstructural characterisation

In this study, LOM and SEM were used for the microstructural characterisation of LP-DED AF Inconel 625 samples. LOM analysis was carried out on a Moticam 1080 BMH equipped with Motic software plus 30 ML for image analysis [2]. This machine has a spatial resolution of 2.8 µm and a focusable lens of 12 mm with a 1 920 × 1 080 high-resolution monitor [2]. LOM was used to characterise the grain structure and the porosity of the Inconel 625 samples. It is the most common and basic instrument for analysing surface microstructures in metallic sample specimens. To quantify the porosity of the Inconel 625 samples, four images were taken at 5× magnification mid-thickness of each sample.

SEM analysis was performed with a Tescan Mira3 machine equipped with a secondary electron detector and a backscattered electron detector for further microstructural analysis [2]. The application of quantitative metallography to SEM mainly focuses on backscattered electrons, electron backscatter diffraction, chemical analysis energy dispersive X-ray (EDX), and volume fraction analysis [6]. The X-ray technique analyses the crystal structure, which identifies the crystalline phases in a particular place of the sample and determines the chemical composition information [7]. An EDX spectrometer was used to determine the chemical composition of the Inconel 625 samples in terms of percentage by analysing the characteristics of the X-rays.

1.5 X-ray diffraction

X-ray diffraction (XRD) analysis is a non-destructive experimental technique for analysing the molecular structures of organic and inorganic compounds [11]. XRD analysis is a rapid technique used for identifying the phases of a crystalline material and determining the crystal orientation, chemical composition and physical properties thereof. Therefore, XRD was used to identify and characterise the phases in the virgin powder and the AF Inconel 625 sample.

The microstructural phase was performed by a multipurpose X-ray diffractometer D8 ADVANCE coupled with Cu-Kα radiation at 40 kV and 40 mA operating with a continuous scan mode. The measurements ran within a range of 2θ with a typical step size of 0.034° in 2θ. The scanning was performed over the range and was recorded at a speed of 0.5 sec/step of the 2θ = 20°−100° range to determine the diffraction peaks.

1.6 Mechanical properties characterisation

MAM materials are still not completely understood and MAM literature mostly focuses on tensile behaviour and microhardness. These mechanical properties are the most common properties used for comparison with traditionally manufactured materials (wrought and cast). Both the orientation and location of sample specimens are important during testing and should thus always be mentioned and reported when evaluating experimental and MAM mechanical results. Additional factors to consider include porosity, residual stress, thermal history, and microstructural characteristics. Porosity – both spheres and irregular shapes – in MAM components or parts reduces the cross-sectional area of the materials, affecting the mechanical properties, which is notable in the reduction of elongation [4-6]. Residual stress can also lead to early failure in MAM parts if a post-non-stress-relieving process is not applied; furthermore, part of the thermal history is important for precipitate-hardened alloys. The columnar grains in most MAM alloys indicate that grain orientation and mechanical properties have a relationship and mechanical anisotropy, which must be considered [14].

MAM nickel-based alloys are complex alloys due to the substantial number of chemical elements, which have different secondary phases that affect the mechanical properties of the product. Thus, the AF microstructure of nickel-based alloys is practically dependent on their chemical composition and thermal history thereof [15]. Hardness is classified as a mechanical property that withstands a material's plastic deformation. A material's hardness measurement can be classified using three methods, namely indentation hardness, rebound hardness, and scratch hardness [16]. Indentation hardness was a concern for the AF Inconel 625 specimens – both parallel and perpendicular to the building direction.

Indentation hardness measurements were conducted to determine the strength of these sample specimens. Hardness was measured using the Rockwell hardness scale. For each sample, both parallel and perpendicular, a load of 10 kg and a dwell time of ±10 seconds were applied, and at least six indentations were performed to obtain reliable results.

2 Results and Discussion

The polished samples were made conductive using a coating in order to enable or improve the imaging of the samples. Applying the correct amount of coating reduces thermal damage, which improves the secondary electrons during analysis. Figure 3 and Figure 4 illustrate the LOM and SEM micrographs of sample specimens of Inconel 625, respectively, both parallel and perpendicular to the building direction.

2.1 Metallographic studies

2.1.1 Light optical microscope

Micrographs of Inconel AF sample specimens are helpful to gain an insightful understanding of the MAM process for layer-by-layer orientation. Figure 3a and Figure 3b respectively illustrate the Inconel 625 parallel and perpendicular to the building direction with laser

movement direction, porosities (spherical and irregular shapes) and layer-by-layer building orientation. Micropores with small spherical and larger irregular shapes were observed in samples – both parallel and perpendicular to the build direction as illustrated in Figure 3a and Figure 3b, respectively [2].

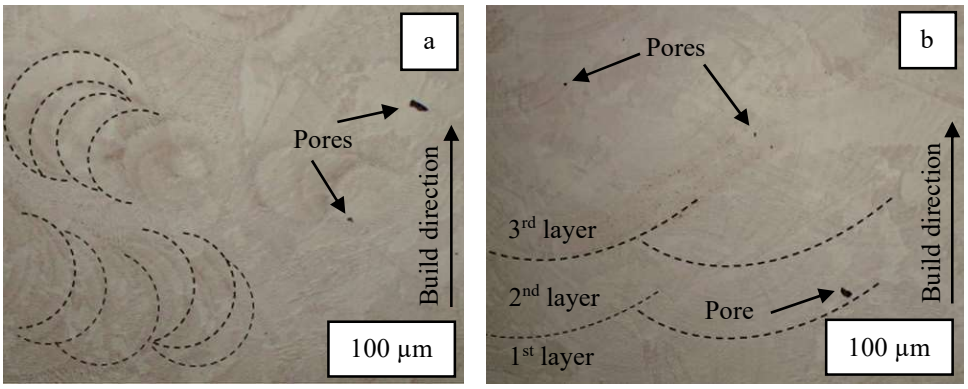

Fig. 3. LOM micrographs of Inconel 625: **a)** Parallel with arc shaped beads and porosities (irregularly shaped); and **b)** Perpendicular with melted track layers patterns and porosities (spherical and irregular shapes) denoted with arrows.

Figure 3a illustrates the bead morphology parallel to the building direction. Bead morphology is common in multi-pass welds in laser powder bed fusion (L-PBF). The bead size with non-uniform multi-pass welds is slightly larger close to the substrate with a smaller bead size at the top layers. The difference in the slightly larger bead size may be attributed to the rapid cooling rates in the first two layers, which are closer to the substrate.

The laser-melted track layers are visible in the scanning pattern in Figure 3b perpendicular to the building direction [2]. The individual melt pool boundaries are visible where the two tracks meet. The overlaps between the tracks were caused by the laser movement forming each layer during the layer-by-layer building process [2]. The overlaps in each layer may be considered high-stress regions because the overlaps face rapid reheating and solidification [2].

The lack of fusion porosity transpired when the molten pool that formed during fabrication could not melt fully in the neighbouring tracks, which resulted in flat cracks perpendicular to the building direction [17]. The small spherical porosity was caused by insufficient fusion and is related to the use of inert gas during the melting pool stage and gas trapped inside the powder, which cannot escape from the melting pool [2], [12-15]. The larger irregular shaped porosity occurred due to an insufficient energy intake to melt the powder for LP-DED, selective laser melting and wire for laser wire-directed energy deposition (LW-DED) during the layer-by-layer fabrication process and may lead to unmelted regions [2], [14-15]. This happened due to the reduction of heat from the feedstock energy and scanning rate, mass flow rate accumulation, or a consolidation of these variables [19]. The tips of irregularly shaped pores may introduce local stress during loading, which could result in early fracture or failure of parts, especially for the side perpendicular to the build direction [2, 20]. Both types of porosity can be reduced by selecting the process parameters carefully. The proper scan speed, scan pattern and laser power parameters must be chosen to have a melt pool that melts at least two to three layers of the substrate to avoid the keyhole pores effect [2], [13-14].

2.1.2 Scanning electron microscopy

The distinction in grain size and direction of the sample specimens shown by SEM analysis in Figure 4a and 4b, respectively, indicate that the grains have a preferred growth direction [2]. The average grain size parallel to the building direction is smaller than the average grain size perpendicular to the building direction illustrated in Figure 4a and Figure 4b, respectively [2]. This indicates that the preferred grain growth direction of these MAM samples is normal to the building direction, which means that the grains are smaller in the direction of the laser motion [2]. This suggests that there may be a connection between the crystallographic orientation and mechanical properties [2, 24]. The grain orientation of Inconel 625 is parallel and perpendicular, as illustrated in Figure 4a and Figure 4b. The grain has texture, meaning it has a preferred direction [2].

Figure 4a parallel to the building direction illustrates two distinct regions, and both cellular and columnar grain structures can be observed. The melting pool boundaries indicate that these two regions have different grain structures due to their different histories and thermal cooling rates during solidification [25]. Figure 4b perpendicular to the building direction illustrates a columnar grain structure with elongated cells. This grain morphology causes a heat-affected zone (HAZ) or laser overlapping zone with a relatively lower cooling rate. Materials with smaller grain sizes increase tensile strength and may increase ductility, whereas materials with larger grain sizes improve high-temperature creep properties [2, 12].

Figure 4c illustrates the HAZ in Inconel 625 perpendicular to the build direction. The HAZ near or in the substrate was neglected because the focus was on the HAZ between the overlapping layers. The dotted lines (region) in Figure 4c indicate the melting pool contours that affect the grain structure and orientation during the next layer process indicated in melted pool 1 and melted pool 2, respectively. HAZ and liquation cracking transpire when the solidified material alongside the fusion zone is exposed to different temperatures, which results in partial melting of the material microstructure or partially melted zone [26].

Two mechanisms cause HAZ liquation cracking, namely melt penetration and solute segregation [27]. Furthermore, the grain structure in Figure 4c illustrates melted pool 1 with columnar grains and melted pool 2 with columnar-dendritic grains. The solidification structure in MAM with metals can be cellular, columnar-dendritic, equiaxed-dendritic, or planar. This is determined from the temperature gradient (G) and grain solidification rate (R) during fabrication processes with respect to the relationships derived from Equations 1, 2 and 3, respectively [19].

The relationships for the cooling rate, thermal gradient and solidification front velocity are as follows:

$$\text{Cooling rate:} \quad \frac{\partial T}{\partial t} \tag{1}$$

$$\text{Thermal gradient:} \quad G = |\nabla T| \tag{2}$$

$$\text{Solidification front velocity:} \quad R = \frac{1}{G}\frac{\partial T}{\partial t} \tag{3}$$

where T is temperature and t is time.

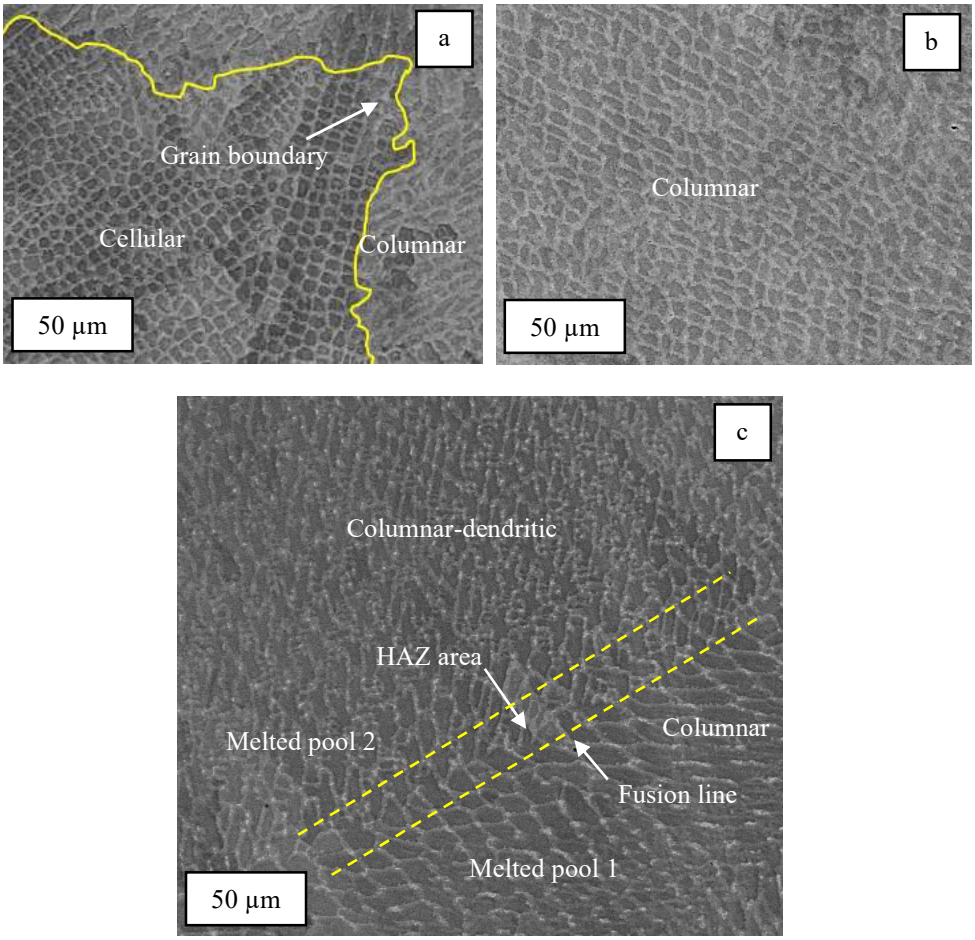

Fig. 4. SEM micrographs of Inconel 625: **a)** Parallel to the build direction with cellular and columnar grain structure with grain boundary; **b)** Perpendicular to the build direction with columnar grain structure; and **c)** Perpendicular to the build direction with HAZ denoted with dotted region, melted pool 1 with columnar grain structure, and melted pool 2 with columnar-dendritic grain structure.

2.2 Energy dispersive X-Ray

The results of Inconel 625 in Figure 5 illustrate spectra 1–5, respectively, in different areas of the AF samples. EDX analysis was used to determine the combined chemical element averages listed in Table 3. The chemical elements prominent in Inconel 625 were 55.76% nickel, 20.72% chromium, and 9.65% molybdenum. Nickel-molybdenum-chromium alloys in this category are known for their high strength despite their high temperatures and corrosive environments [2].

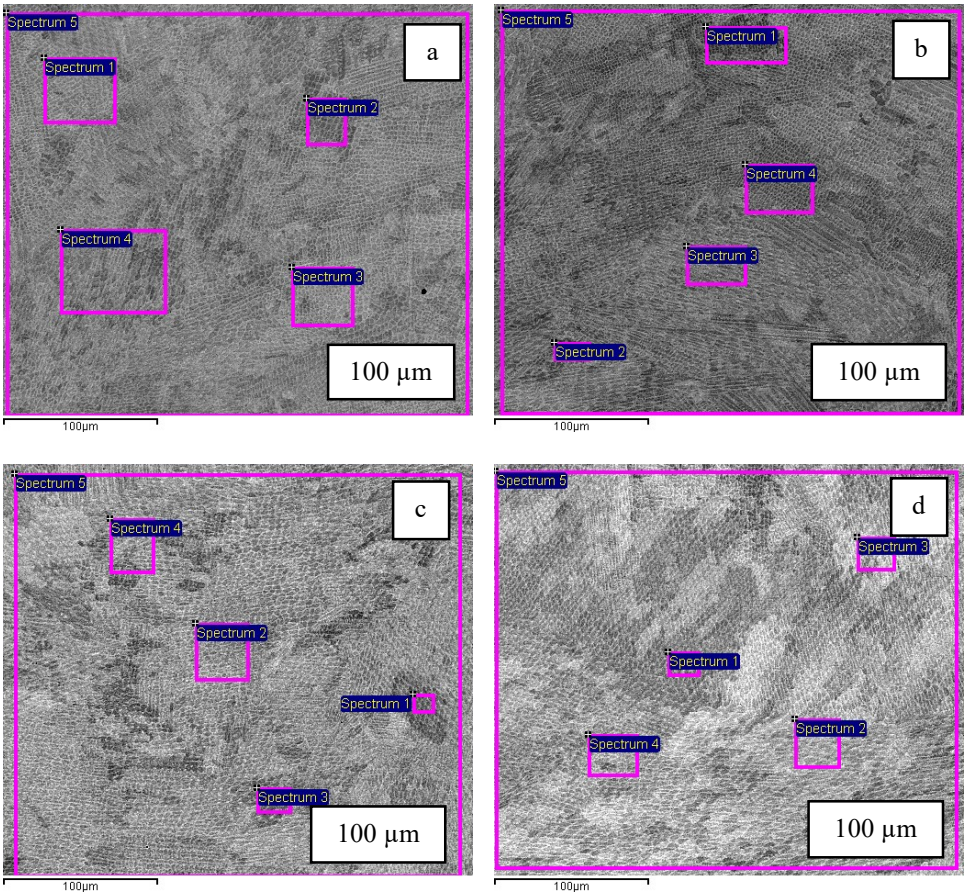

Fig. 5. EDX of Inconel 625: **a)–b)** parallel, and **c)–d)** perpendicular to spectra 1–5 in different areas of each sample to the building direction, respectively, all with the same magnification.

Table 3. Chemical results for Inconel 625 virgin powder, 400 W with 10.58 mm/s AF sample compared with nominal composition (wt%) [20, 21].

Element wt%	**Al**	**C**	**Co**	**Cr**	**Cu**	**Fe**	**Mn**	**Mo**	**N**
Virgin powder	<0.01	0.01	<0.1	21.4	0.03	3.4	0.25	8.7	0.09
Nominal	0.4 max	0.1 max	–	20–23	0.5 max	5 max	0.5 max	8–10	–
400 W, 10.58 mm/s	–	6.71	–	20.72	–	3.19	–	9.67	–
Element wt%	**Nb**	**Ni**	**O**	**P**	**S**	**Si**	**Ta**	**Ti**	
Virgin powder	3.23	62.34	0.0185	0.001	0.004	0.40	<0.00050	<0.01	
Nominal	3.2–4.1	58	–	0.02	0.015 max	0.5 max	–	0.4 max	
400 W, 10.58 mm/s	3.59	55.76	–	–	–	0.53	–	–	

The LP-DED process demonstrates that the values for nickel and chromium decreased from those seen in the supplied powder and nominal values (nickel: 62.34 wt%, 58 wt%, 55.76 wt%; chromium: 21.4 wt%, 21.5 avg. wt%, 20.72 wt%). The element iron decreased from the supplied powder value of 3.4 wt% to 3.19 wt% with a nominal value of 5 wt%. The only concern value was the increase of the carbon element for supplied powder and nominal composition (0.01 wt%, 0.1 wt%), respectively, which increased to 6.71 wt% during the LP-DED process. The vaporisation of chemical elements occurred during MAM in the molten pool at elevated temperatures. The reduction of these chemical elements can be attributed to the vaporisation under laser processing.

The boiling points of these elements under standard pressure for nickel, chromium and iron were 2 839°C, 2 665°C and 2 857°C, respectively [29]. These boiling points were among the lowest in the alloy. The boiling point of carbon was among the highest in the AF sample with a value of 4 827°C under standard pressure and among the highest vaporisation temperatures under various pressures (torr) ranging from 10^{-5} torr to 1 torr as illustrated in Table 4.

The high boiling point value, LP-DED energy condition, and high vaporisation temperatures could have attributed to the increase in carbon during fabrication. Furthermore, the minimal increase of some of the other elements' values from the supplied powder during DED process is due to their increased concentration because of the losses of the decreased elements. These vaporisations of chemical elements may affect the mechanical properties due to the change in microstructure and possible deterioration of corrosion. It is important to remember that all elements do not vaporise at the same rate during fabrication processing, and the selective vaporisation of elements often result in an alloy changing composition.

The role of an inert gas inside the building chamber during the LP-DED process is to remove the by-products and air in the process chamber and to protect against oxidation [30]. There are different gas supply options for MAM. This study used argon gas as the inert gas during the fabrication process. The oxygen and nitrogen showed a complete vaporisation in the AF sample compared with the virgin powder chemical composition during the fabrication process. The nominal composition had no oxygen and nitrogen chemical elements. The amount of argon atmosphere inside the building chamber was most likely the cause of the vaporisation of oxygen and nitrogen during the fabrication process. The gas sensor measured the argon atmosphere in the building chamber to be approximately 50–100 ppm during fabrication.

Table 4 shows the vapour pressure data for the selected elements relevant to PBF. An important observation can be made regarding PBF process control. In the 10^{-5} torr to 10^{-4} torr vacuum range, all elements except aluminium had vaporisation temperatures lower than their respective melting points. In the 10^{-3} torr to 10^{-2} torr range, the vaporisation temperatures of most elements exceeded their melting points except for carbon, chromium, manganese and iron. In the 10^{-1} torr to 1 torr range, the vaporisation temperatures of the majority of the elements also exceeded their melting points except for carbon, chromium and manganese. Therefore, based on the composition element used to fabricate the Inconel 625 sample specimen, the fabrication process should be managed under limited pressure to minimise vaporisation during LP-DED processing [31].

Table 4. Vaporization temperature of selected elements as a function of pressure, adapted from [29,31].

Element	Tm	Tb	Vaporization temperatures at various pressures (torr)						
			10^{-5}	10^{-4}	10^{-3}	10^{-2}	10^{-1}	1	760
Al	659	2 447	882	972	1 082	1 207	1 347	1 547	2 467
C	3 350	4 827	–	2 290	2 421	2 681	2 926	3 214	4 827
Co	1 495	2 877	1 162	1 262	1 377	1 517	1 697	1 907	3 097
Cr	1 903	2 665	1 062	1 162	1 267	1 392	1 557	1 737	2 222
Cu	1 084	2 578	942	1 032	1 142	1 272	1 427	1 622	2 595
Fe	1 539	2 857	1 107	1 207	1 322	1 467	1 637	1 847	2 727
Mn	1 244	2 051	697	767	852	947	1 067	1 227	2 097
Mo	2 577	4 827	1987	2 167	2 377	2 627	2 927	3 297	4 804
Nb	2 477	4 927	–	–	–	–	–	–	4 742
Ni	1 452	2 938	1 142	1 247	1 357	1 497	1 667	1 877	2 837
P	44.1	280	–	–	160	190	225	265	431
S	–	444.6							444
Si	1 415	2 787	1 177	1 282	1 357	1 547	1 717	1 927	2 477
Ta	3 020	5 457	–	2 599	2 820	3 074	3 370	3 740	6 027
Ti	1 660	3 287	1 321	1 431	1 558	1 703	1 877	2 083	3 127

Tm = melting temperature; Tb = boiling temperature.

2.3 X-ray diffraction

Bragg's Law for interplanar spacing data was used to determine the diffraction results of the virgin Inconel powder and the AF Inconel 625 sample specimens. The phases were identified with the Briggs diffraction by matching the calculated peaks until all phases were present Bragg's diffraction occurs when the radiation of a wavelength is similar to atomic spacing, which is scattered by atoms of crystalline systems, and results in constructive and destructive interference [2, 11].

The Bragg diffraction analysis was determined based on the resulting wave interference pattern of the crystallographic planes in the crystal lattice [2]. To determine the d-spacing and lattice parameters, the XRD and scan parameters during the analysis were the same for the GA virgin powder and the AF sample. Figure 6a and Figure 6b illustrate the powder and AF sample intensity vs diffraction angle during XRD analysis, respectively. Table 5 lists the crystallographic parameters of the GA virgin powder and the AF sample.

Therefore, according to Bragg's Equation:

Bragg's Law

$$n\lambda = 2d\,sin\,\theta\ (n = 1, 2, 3,\ldots.) \qquad (4)$$

where n= positive integer (order of diffraction), λ = incident wavelength, d = interplanar distance between atoms inside the material, and θ = scattered angle [2].

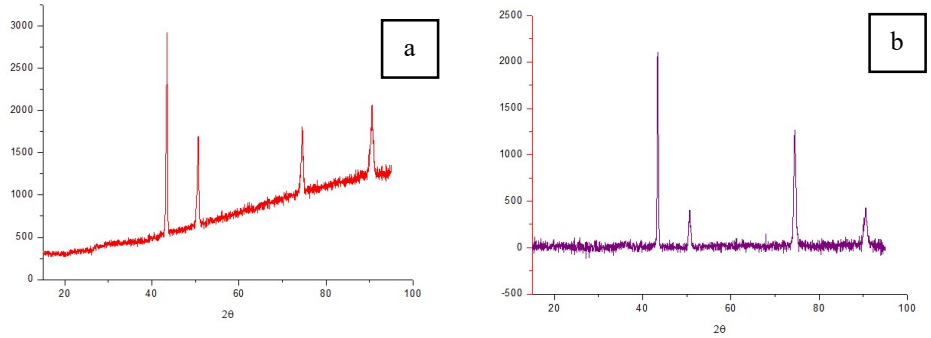

Fig. 6. XRD pattern of Inconel 625: **a)** Powder intensity vs diffraction angle; and **b)** AF sample intensity vs diffraction angle.

Table 5. Crystallographic parameters of GA virgin Inconel 625 powder and AF-DED sample.

Powder type	**Inconel 625 samples**	**Peak position for crystallographic planes**				**d-spacing for (111) plane [Å]**	**Lattice parameter [Å]**
		111	200	220	222		
GA	Virgin powder and AF	44.45°	50.64°	74.48°	90.46°	2.040	3.536

The XRD results of the virgin Inconel powders and AF specimens are illustrated in Figure 6a and Figure 6b, respectively. The peaks corresponded to the lattice planes in this superalloy, which was used for phase identification. The powder and AF specimens in Figure 6a and Figure 6b, respectively, illustrate that the outstanding peaks are related to the face-centred-cubic (FCC) lattice γ-nickel phase [32].

The lattice parameters corresponded to the FCC phases, with the strong first peak crystal structure (111) parameter of 3.536 Å, second peak crystal structure (200) and third peak both a parameter of 3.600 and fourth peak (222) crystal structure of 3.760 Å, respectively within the samples. The (111) peak is typically the most intense peak in the XRD pattern and is often used as the reference peak for indexing the crystal structure.

The presence of the (111) peak indicates that the sample has a strong and specific crystal structure along the (111) plane and gives an indication of the orientation of the crystal lattice [11, 32]. The second peak (200) is the second strongest peak and corresponds to the crystallographic plane of FCC. The third peak (220) provides information about the arrangement of atoms in the crystal structure in different directions. The (200) and (220) planes have the same lattice parameters as mentioned, which indicates that these planes have a slight deviation with respect to the reference peak. The peak at (222) also corresponds to the crystallographic plane of FCC. This indicates that the material has a well-defined crystallographic structure in the (222) direction [11, 32]. However, the lattice parameter of

this peak is notably different from the reference peak at (111). This suggests that there may be distortion or lattice strain in the (222) direction [33, 34]. The peak shift on the 2θ scale for the AF Inconel 625 samples indicate that the lattice parameters increased due to thermal expansion, which resulted in the atomic radius increasing.

The XRD spectra for the powder and AF sample corresponded to a difference in the intensity peaks of virgin powders and AF samples. In Figures 6a and Figure 6b, respectively, the intense peak (200) of the virgin powders was higher than the AF-DED peak (200) and the AF LP-DED peak intensity (220) was higher than the virgin power peak (220). The peak intensity of virgin powder (222) was higher than the AF sample. The peak shifts were caused by the change of crystal lattice shifts to higher angles during the XRD analysis due to compression of the crystal lattice [33]. The variation in peak intensity could reveal useful information about crystallography orientation and developed texture in LP-DED fabricated parts.

The lattice parameters and d-spacing during XRD will give insight and understanding of the precipitation or dissolution of intermetallic and carbides in Inconel 625 without affecting the precipitates form the matrix [34]. Furthermore, the nature of precipitation can be identified from the lattice parameters.

3 Mechanical Properties: Microhardness Test Results

The Rockwell microhardness of the AF specimen Inconel 625 and indents were taken 5 mm from either side of each specimen from the first indent centre and two indents 5 mm above and below the centre as illustrated in Figure 7.

Fig. 7. Number of indentation values (location) on samples vs Rockwell hardness.

The microhardness of the first and second indentations for both the parallel and perpendicular Inconel 625 is near the substrate and first few layers, whereas the third and fourth indentations were in the centre layers, and the fifth and sixth indentions were near the last layers. The microhardness of both the parallel and perpendicular samples changed along the building direction variation in the microstructure. The microhardness parallel to the building direction in Figure 7 illustrates that the microhardness is on average higher in the central and last layers. The microhardness perpendicular to the building direction is on

average higher in the first layers and last layers. Furthermore, Figure 7 illustrates that both samples have a wavy profile. The inhomogeneity of the microstructure could have been attributed to the wavy hardness results in both the parallel and perpendicular samples, respectively, which were caused by the cyclic thermal history that varied during processing [19].

The average microhardness of the AF samples parallel and perpendicular to the building direction was 98.8 HRB and 101.6 HRB, respectively. The average hardness for both the parallel and perpendicular samples was similar to the hardness values reported by Gamon et al., Marchese et al., and Wong et al. [34-36]. The microhardness for both parallel and perpendicular samples is slightly lower in the central region of each sample as illustrated in the Figure 7 indentation. Dass and Moridi, Kistler et al., and Shamsaei et al. also reported that the average microhardness in the central region was lower than the first and last layers post the LP-DED process [19], [37-38]. Furthermore, a higher interlayer dwelling time with a higher thermal gradient may also increase hardness [19].

4 Sample Defects

Even though MAM fabrication has many advantages compared with conventional or traditional fabrication methods, MAM also has common defects, such as unmelted powders during fabrication, porosity in samples, process cracking, delamination, surface roughness, spatter, and residual stress. Possible defects that may occur during powder production include satellites and internal porosity.

4.1 Defects of Feedstock material and As-fabricated sample

Figure 8a illustrates the powder morphology with spherical and deformed particles with satellites obtained with SEM. These surface deformations, namely irregularly shaped particles and satellites, are classified as surface defects that are caused by differences in the solidification rate between the partially smaller and larger molten particle sizes [40]. Research reported by [6-11, 21] showed that GA powder has spherical powder particles and deformed particles with satellites. An internal powder porosity analysis was not conducted, but the section view of GA powders was reported by [45], which showed pores and irregular particles due to particle joining and collision during solidification

From the above-mentioned sample defects, the AF samples had post-processing spatter, surface defects and gas pores in the sample parallel and perpendicular to the building direction as illustrated in Figure 3a, Figure 3b, Figure 8b, Figure 8c, Figure 8d and Figure 8e, respectively. Spatter cannot be prevented during the fabrication process in L-PBF, DED and conventional laser welding. Spatter behaviour has a correlation with L-PBF and DED, which are complex heat transfer processes that lead to metallurgical defects and degrade mechanical properties [31-33].

Figures 1c and Figures 8b illustrate spatter build-up during the LP-DED process in the *x*, *y* and *z* direction respectively, as well as an edge defect. Spatter has an unfavourable effect during fabrication stability, and the efficiency of the laser influence and diminish the characteristics of the fabricated component sample and may damage the machine [49]. The process mechanism of oxidised spatter has an unfavourable effect on metallic powder recoating and energy absorption during laser powder bed fusion (L-PDF) and DED processes [49]. Furthermore, spatter particles formed during fabrication redeposit into the powder bed during recoating; the voids between the powder and spatter particles may cause part defects [50].

Figure 8b illustrates the blobs and zits on the AF sample that appear when the laser beam switched direction. It creates an extra deposition during the unsuitable dwelling time when the melting pool overlaps. Overlapping occurs at the start and finish position during the fabrication process as overlapping cannot be a seamless process. In addition, edge defects may also occur as either an underlay or overlay on opposite sides of the AF material [51]. This results in an uneven level with the building plane that varies in height from the AF part or component.

There are two types of porosities in MAM, namely intralayer (spherical pores) and interlayer (irregular pores) [19]. Figure 3a and Figure 3b illustrate the LOM images of spherically and irregularly shaped pores, whereas Figure 8c and Figure 8d illustrate the SEM images of spherically shaped pores in the AF samples. The spherically shaped pores in Figure 3b and Figure 3c, and Figure 8c and Figure 8d, respectively, stem from possible powder contamination, voids or melting after layer deposition [45].

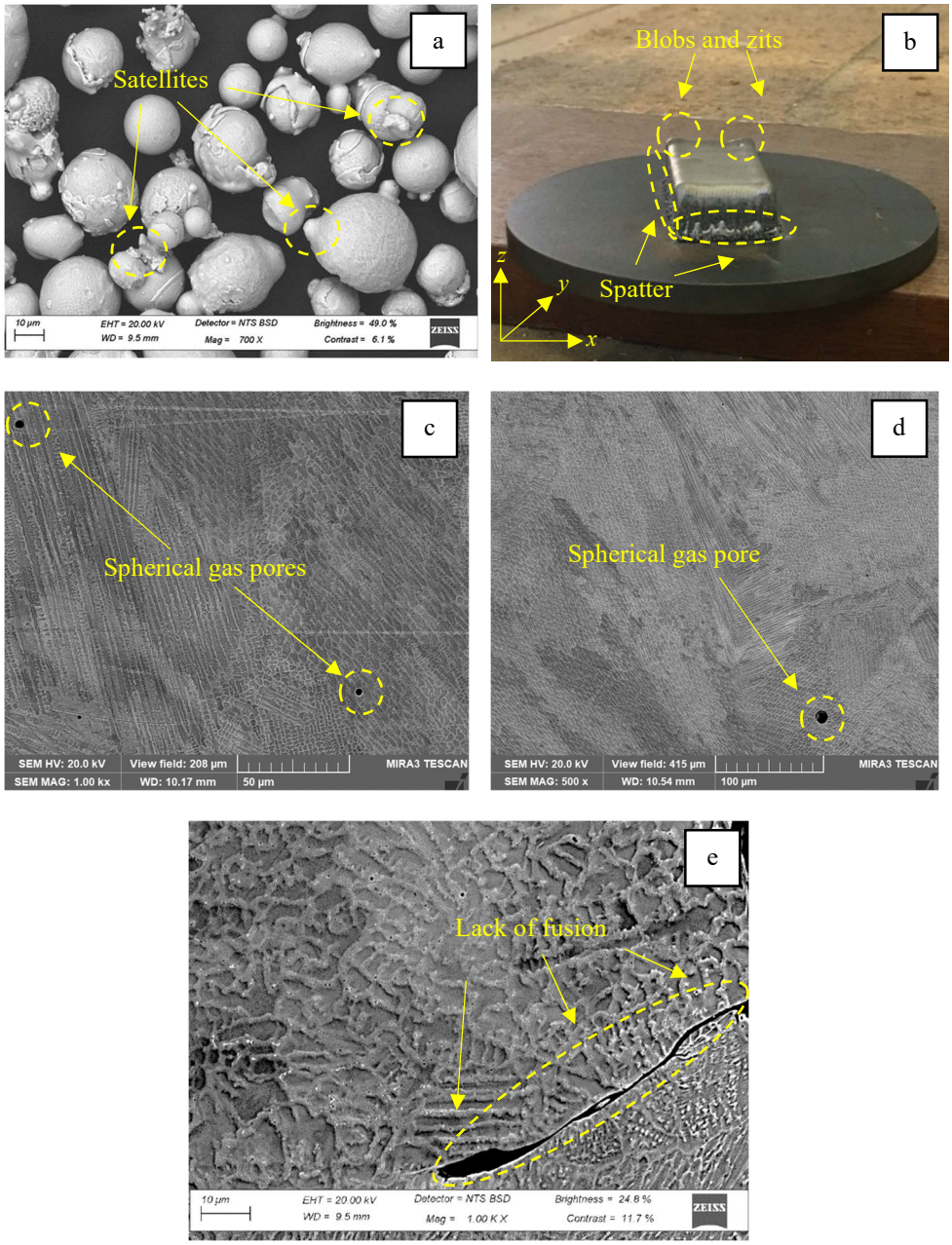

Fig. 8. a) Surface morphology and defects of GA virgin Inconel 625 powders; **b)** Fabrication spatter and development of blobs and zits; **c)** Spherical gas-shaped pore parallel to the building direction; **d)** Spherical gas-shaped pore perpendicular to the building direction; and **e)** Lack of fusion. Figures 8a, 8c, 8d and 8e have different magnifications.

Figure 8c and Figure 8d show that the spherically shaped pores are in random sections, parallel and perpendicular to the AF samples. The spherically shaped porosity transpires when gas bubbles are entrapped in the molten metal bead before solidification or they are caused by a high laser scan speed during the fabrication process [52]. Dass and Moridi also reported that spherically shaped pores occurred in random locations and were observed in regions with lower solidification rates [19]. Irregularly shaped pores occur due to insufficient energy intake to melt the LP-DED or LW-DED during the layer-by-layer fabrication process, which may lead to unmelted regions [19].

In Figure 3a, the irregularly shaped pores were between the layers, whereas Figure 8b illustrates that the irregularly shaped pores were between the first couple of layers and near the substrate in the building direction. Spherical pores may cause less damage to the mechanical properties of the MAM parts, whereas irregular pores raise the concentration of stress that may lead to failure [8]. Figure 8e illustrates the lack of fusion: these defects occur when the energy delivered during the fabrication process is insufficient, which causes layers to fuse incompletely, or the new layer and previous layer not to overlap sufficiently [40, 41]. Furthermore, the width of the melting will be small if the laser energy is too low, and insufficient overlay between scanning tracks may occur.

5 Conclusion

In summary, the AF LP-DED Inconel 625 sample was fabricated successfully with selected process parameters with virgin Inconel powder to investigate microstructure evolutions, EDX, XRD, material hardness and defects of the virgin Inconel 625 powder and AF sample specimens. Based on the results, the following primary conclusions were drawn from this investigated research:

a. The sample parallel to the building direction had a cellular and columnar grain microstructure. The sample perpendicular to the building direction had a predominately columnar and dendritic-columnar microstructure. The melting pool between the layers affects the grain size, grain structure and orientation due to HAZ.

b. EDX analysis and metallography confirmed the chemical composition and uniform structure of the AF sample, with nickel, chromium and molybdenum as the prominent chemical elements. In addition, the EDX analysis results demonstrated that compared with the supplied virgin powder, the composition of some chemical elements of the AF sample had increased due to the high boiling points and high vaporisation temperatures, whereas some decreased due to the lower boiling points and lower vaporisation temperatures.

c. The phase structure during XRD of the virgin powder and AF sample corresponded to and predominately composed of the γ-Ni (FCC) phase with a lattice parameter of 3.536 Å for (111).

d. The average microhardness for the AF samples, parallel and perpendicular to the building direction, was 98.8 HRB and 101.6 HRB, respectively. Research reported by Dass and Moridi showed that increasing the substrate thickness of the AF-DED process increases the material hardness and finer microstructure as the thicker substrate has the potential to absorb heat faster during the fabrication process [19]. A hardness study of the DED fabrication process stated that alloy elements selection or post-processing (heat treating or ageing) of MAM components or parts has more control over material hardness than changing process parameters [15].

e. Spatter occurred during the fabrication process on the substrate in the *x* and *y* directions. Spatter is an unpreventable fabrication defect caused by the heat transfer process. Spatter degrades a material's mechanical properties and reduces the quality of fabricated parts or components. Post-processing is essential to remove spatter and enhance surface quality. Mechanical properties may improve and less spatter may occur during the LP-DED fabrication if the process parameters are adjusted.

f. General GA powder defects with surface deformation resulted in irregularly shaped powder particles with satellites caused by different solidification rates during production. The particle size ranged from 20 μm to 50 μm, which included near perfectly spherical and irregularly shaped powder particles. There were general defects in AF samples with spherical and irregular pores. The spherical pores were in random locations in both samples, whereas the irregularly shaped pores were in the first couple of layers.

The results obtained in this research paper demonstrated that LP-DED MAM technology with a low fabrication rate has great potential for prototyping and is suitable for various industrial sectors. However, additional research is required on AF parts to adjust the process parameter variables, including laser beam size, laser power, scanning speed, powder feed rate, and scanning strategy, that affect the mechanical, metallurgical and geometrical properties as well as residual stress.

Understanding the root cause of defects in LP-DED is critical for improving quality and consistency during fabrication. Adjusting these variables may also reduce defects in LP-DED samples in order to achieve optimal results, which will be extremely beneficial to LP-DED MAM processing. Furthermore, research should also be conducted on the mechanical tensile properties at elevated thermal temperatures to improve material characteristics. This additional research is currently planned.

6 Data Availability

The data used to support the findings of this study are included in the research paper.

7 Conflicts of Interest

The authors wish to declare that there has been no conflict of interest.

References

1. A. Bandyopadhyay, Y. Zhang, S. Bose, Curr Opin Chem Eng, **28**, 96–104 (2020)
2. T. Booysen, Microstructural effects on properties of additively manufactured Inconel 625 and 718, (M Eng, Cape Peninsula University of Technology, 2019)
3. Y.L. Hu et al., Mater Des, **186** (2020)
4. B.E. Carroll et al., Acta Mater, **108**, 46–54 (2016)
5. L.E. Shoemaker, Alloys 625 and 725: Trends in properties and applications (TMS, Pittsburgh, PA, 2005)
6. J. Dutkiewicz et al., Materials, **13**, 21, 1–17 (2020)
7. ASTM, Standard specification for additive manufacturing nickel alloy (UNS N06625) with powder bed fusion (ASTM, West Conshohocken, PA, 2014)

8. D. Deng, Additively manufactured Inconel 718: Microstructures and mechanical properties (Licentiate thesis, Linköping University, 2018)
9. LPW, Carpenter Addit (2020), https://www.carpenteradditive.com/technical-library/ (accessed Apr. 26, 2020)
10. M. Tlotleng, J Mater Eng Perform, **28**, 2, 701–708 (2019)
11. A. Ali, Y.W. Chiang, R.M. Santos, Miner, **12**, 2 (2022)
12. R.F. Ashton, R.P. Wesley, C.R. Dixon, Weld Res Suppl, **3**, 95–98 (1975)
13. J.F. Rudy, E.J. Rupert, Weld J (NY), **49**, 7, 322s–336s (1970)
14. W.J. Sames, Additive manufacturing of Inconel 718 using electron beam melting; mechanical properties; post-processing; processing (PhD, Texas A&M University, 2015)
15. J.S. Zuback, T. DebRoy, MDPI, **11**, 11 (2018)
16. R.E. Smallman, A.H.W. Ngan, Physical metallurgy and advanced materials engineering, 7th ed (Elsevier, 2011)
17. A. Du Plessis, Addit Manuf, **30**, 100871 (2019)
18. T. Vilaro, C. Colin, J.D. Bartout, Metall Mater Trans A Phys Metall Mater Sci, **42**, 10 (2011)
19. A. Dass, A. Moridi, *Coatings*. 1–26 (2019)
20. B.E. Carroll, T.A. Palmer, A.M. Beese, Acta Mater, **87**, 309–320 (2015)
21. H. Gong, K. Rafi, H. Gu, T. Starr, B. Stucker, Addit Manuf, **1–4**, 87–98 (2014)
22. A. Anam, Microstructure and mechanical properties of selective laser melted superalloy Inconel 625 (PhD, University of Louisville, 2018)
23. N. Ahmed, I. Barsoum, G. Haidemenopoulos, and R. K. A. Al-Rub, J Manuf Process, **75**, 415–434 (2022)
24. O. Sanchez-Mata, X. Wang, J. Muñiz-Lerma, S. Atabay, M. Attarian Shandiz, M. Brochu, J Alloys Compd, **865**, 158868 (2021)
25. C. Tan, K. Zhou, M. Kuang, W. Ma, T. Kuang, Sci Technol Adv Mater, **19**, 1, 746–758 (2018)
26. X. Guo, P. He, & K. Xu, P.Y. Chen, B. Chen, S.B. Huo, Weld World, **65**, 825–832 (2021)
27. J.N. DuPont, J.C. Lippold, S.D. Kiser, Welding metallurgy and weldability of nickel-base alloys (John Wiley & Sons, Hoboken, NJ, 2009)
28. ASTM, Standard specification for additive manufacturing nickel alloy (UNS N07718) with powder bed fusion F3055 (ASTM, West Conshohocken, PA, 2014)
29. H. Osterman, V. Antes, Critical melting points and reference data for vacuum heat treating (Solar Atmospheres Inc, Souderton, PA, 2010), https://solarmfg.com/wp-content/uploads/2011/01/Critical-Melting-Point1.pdf (accessed Nov. 08, 2022)
30. C. Pauzon, E. Hryha, P. Forêt, L. Nyborg, Mater Des, **179** (2019)
31. S. Das, Adv Eng Mater, **5**, 10, 701–711 (2003)
32. F. Azarmi, J. Saaedi, T.W. Coyle, J. Mostaghimi, Adv Eng Mater, **10**, 5, 459–465 (2008)
33. Y. Gao, M. Zhou, Appl Sci, **8**, 12 (2018)
34. A. Mostafaei, J. Toman, E.L. Stevens, E.T. Hughes, Y.L. Krimer, M. Chmielus, Acta Mater, **124** (2017)

35. A. Gamon et al., Results Mater, **12** (2021)
36. G. Marchese, A. Aversa, E. Bassini, Metals, **11**, 6, 929 (2021)
37. H. Wong, K. Dawson, G.A. Ravi, L. Howlett, R.O. Jones, C.J. Sutcliffe, **105**, 2891–2906 (2019)
38. N.A. Kistler, D.J. Corbin, A.R. Nassar, E.W. Reutzel, A.M. Beese, J Mater Process Technol, **264**, 172–181 (2019)
39. N. Shamsaei, A. Yadollahi, L. Bian, S.M. Thompson, Addit Manuf, **8**, 12–35 (2015)
40. C. Zhong, T. Biermann, A. Gasser, R. Poprawe, J Laser Appl, **27** (2015)
41. S.J.C. Pleass, Addit Manuf, **24**, 419–431 (2018)
42. M.N. Ahsan, R. Bradley, A.J. Pinkerton, J Laser Appl, **23**, 2 (2011)
43. Y.N. Zhang, X. Cao, P. Wanjara, M. Medraj, *Fiber laser deposition of Inconel 718 using powders*, in Materials Science and Technology Conference and Exhibition (2013)
44. R. Dawes, J. Bowerman, R. Treplenton, Johnson Matthey Technol Rev, **59**, 3, 243–256 (2015)
45. X. Wang, X. Gong, K. Chou, *Review on powder-bed laser additive manufacturing of Inconel 718 parts*, in Proceedings of the Institution of Mechanical Engineers, Part B: Journal of Engineering Manufacture (2017)
46. W.E. King et al., Appl Phys Rev, **2**, 4 (2015)
47. W.J. Sames, F.A. List, S. Pannala, R.R. Dehoff, S.S. Babu, Int Mater Rev, **61**, 5, 315–360 (2016)
48. A.R. Nassar, M.A. Gundermann, E.W. Reutzel, P. Guerrier, M.H. Krane, M.J. Weldon, Sci Rep, **9**, 1 (2019)
49. S.A. Khairallah, A.T. Anderson, A. Rubenchik, W.E. King, Acta Mater, **108**, 36–45 (2016)
50. Z. Li et al., Micromachines, **13**, 8 (2022)
51. M. Liu, A. Kumar, S. Bukkapatnam, M. Kuttolamadom, Procedia Manuf, **53**, 507–518 (2021)
52. Q. Jia, D. Gu, J Alloys Compd, **585**, 713–721 (2014)
53. S. Cooke, K. Ahmadi, S. Willerth, R. Herring, J Manuf Processes, **57**, 978–1003 (2020)
54. B. Zhang, Y. Li, Q. Bai, Chin J Mech Eng (Eng Ed), **30**, 515–527 (2017)
55. Metal AM, Hot isostatic pressing: Improving quality and performance in AM, https://www.metal-am.com/articles/hot-isostatic-pressing-improving-quality-and-performance-in-3d-printing/ (accessed May 05, 2023)
56. S. Götelid et al., Rapid Prototyp J, **27**, 9, 1617–1632 (2021)

10 October 2023
Theo-Neal Booysen
Department of Mechanical and Mechatronics
Tshwane University of Technology
Staatsartillerie Road
Pretoria West
Pretoria
South Africa
0183

Rebuttal for ‘’Microstructural effects on properties of as-fabricated Inconel 625 with direct energy deposition process’’

Dear Editor

I Theo-Neal Booysen, would like to thank the reviewers for their generous comments on our manuscript ‘’Microstructural effects on properties of as-fabricated Inconel 625 with direct energy deposition process’’. We appreciate the insightful comments and suggestions provided by reviewers. We have carefully considered these comments and have made the necessary revisions to improve the quality and clarity of our manuscript. Below, I provided a point-by-point response to each reviewer's comments.

Review 1:

Comment 1

Research Gap NOT mentioned

Response

The AF LP-DED Inconel 625 sample was successfully fabricated using selected process parameters. The process parameters selected ensured a continuous build with improved dimensional accuracy and minimal operator intervention. The research presented that microstructure-related defects were minimal and that there was a relationship between the defect porosities. Additionally, this research provides insight into how laser processing may affect chemical elements (increasing or decreasing) during fabrication, depending on their vaporisation temperatures as a function of pressure.

Comment 2 (pg. 3)

Powder particle size taken from references not confirmed by their own

Response

The manuscript includes information on the particle size of our powder and has removed details on the powder suppliers.

Comment 3
Reason for selection of mild steel as a substrate
Response
Mild steel was chosen for its low carbon content and moderate thermal conductivity, allowing for fast heat absorption as substrate and reducing the risk of warping, cracking or distortion during the fabrication LP-DED process.

Comment 4 (pg. 4)
Why spatter formation only in Lower layer as shown in figure 1 a.
Response
The lower layers during the MAM fabrication process typically receive more heat, the overlapping, powder interaction and thermal interaction, cooling and solidification which is a complex heat transfer process during the fabrication process. Furthermore, spatter cannot be completely prevented during laser-based manufacturing processes such as L-PBF, DED, and conventional laser welding. However, it can be minimised by adjusting process parameter variables : laser beam size, laser power, scanning speed, powder feed rate, scanning strategy and gas flow rate .

Comment 5 (pg. 5)
Benchmark or pre-investigation experiment process for selection of process parameter.
Response
The parameters were identified based on the process development design of experiments (DOE) conducted on stainless steel materials with similar behaviour to that of Inconel 625. The selected parameters for fabrication were those that ensured a continuous build with improved dimensional accuracy and minimal operator intervention.

Comment 6
Extent of effect of thermal-compression mounting.
Response
The samples were mounted using a hot mounting process, both parallel and perpendicular to the building direction. Pressure and heat were used to encapsulate the as-fabricated samples for grinding and polishing. The mounted samples in resin were analysed with LOM and SEM to characterise the microstructure of LP-DED as-fabricated Inconel 625 samples.

Comment 7
Keyhole effect and Bow shock effect
Response
Keyhole effect
This keyhole effect refers to the shape of the pores that may occur within the first layers of the fabricated sample during layer deposition.

Bow shock effect

The bow shock effect is a phenomenon that occurs during cold spray deposition on a single track. The height of the bow shock is influenced by various factors such as operating pressure, substrate thickness, and material (AM,2020). LP-DED is a similar technology to cold spray, but with LP-DED, deposition can be done at different angles, while cold spray requires a perpendicular nozzle during deposition. Although the bow shock effect was not considered in this manuscript and was not included in my literature review and results, it could be explored in future research papers.

https://www.metal-am.com/articles/how-metal-3d-printing-is-going-supersonic-at-spee3d/ (accessed 9 October 2023)

Comment 8 (pg.8)

Section 2.21: How smaller grain size lead to increase in DUCTILITY.

Response

A material with a smaller grain size tends to be more flexible and can be stretched or elongated more easily. This is because the smaller grain size means there are more grain boundaries per unit volume which allows the material to deform without immediately fracturing. Additionally, reducing the grain size in a material can minimize the presence of brittle phases within the material boundaries, thereby increasing the ductility of the material.

Comment 9

How high vaporisation temperature could have attributed to an increase in Carbon during fabrication.

Response

As mentioned on page 7 of our manuscript, carbon is a chemical element with the highest melting and boiling temperatures among all the other chemical elements in the virgin supplied powder. Other chemical elements will reach their melting and boiling temperatures before carbon during the fabrication process. As a result, the vaporised carbon can mix with the molten pool of other chemical elements during fabrication at elevated temperatures within the building chamber, leading to an increase in carbon within the as-fabricated sample.

Comment 10 (pg.11)

Validation for: Increase in concentration of one element by decrease in another?

Response

As mentioned in response to comment 9, vaporization of chemical elements is common during MAM (metal additive manufacturing) based on the melting and boiling temperatures of the chemical elements within the alloy. Some chemical elements will either increase or decrease within the alloy depending on their melting and boiling temperatures. Elements with higher melting and boiling temperatures will increase, while elements with lower melting and boiling temperatures will decrease during the fabrication process. In summary, the vaporisation temperature of selected elements as a function of pressure may be attributed to the increased concentration of one element by a decrease in another at elevated temperatures.

Comment 11 (pg.12)
Claim: High-stress region of overlap face: how to overcome these stress?
Response
During the fabrication process, high-stress regions can occur when there is an overlap. To reduce these stresses, there are several adjustments one can make including process parameters, component design, material selection, scanning strategy, and possible stress relief passes like preheating the substrate before fabrication.

Review 3:
Comment 1 (pg. 1)
A brief overview of your results is missing here, although not critical it will give the reader some high-level summary of your findings
Response
A brief overview of my results was included in my abstract
Comment 2 (pg. 11)
In general bulk measurement techniques give different results to EDS which focuses on a very localised area
Response
The chemical composition of the virgin powder and the nominal and process parameters of the as-fabricated sample specimens are shown in Table 3. The EDX results were obtained from Figure 5 a-b and c-d of spectra 1-5, which were taken from different areas of each sample, both parallel and perpendicular to the building direction. The key finding was that the chemical element's weight percentage(wt.%) during laser processing may decrease or increase, depending on their melting and boiling temperatures. The results of the EDX analysis on the as-fabricated samples provide a general overview and do not focus on any specific area of the sample specimen. Further research can be carried out to analyse specific areas of the sample specimen.

Comment 3 (pg.11)
You need to compare apples with apples. Use ICP to confirm the composition.

Response

This comparison of the chemical element of carbon (C) was inserted in the section above on pg. 11, where virgin powder (ICP results), nominal (ICP) and process parameters of the as-fabricated sample specimens chemical composition results were discussed.

Comment 4 (pg.13)

This does not sound right and how do you measure Ar?

Please just review carefully and rephrase this

Response

The sentence has been rephrased, and it now mentions the measurement instrument used for argon gas (Ar).

Comment 5 (pg.13)

This is a little bit generic - you need to explain your results - go into detail about what we are seeing in the peaks

Response

The crystallographic planes were explained in detail, based on the peaks present in the XRD results.

Comment 6 (pg.13)

Where are these results that you refer to?

Response

The sentence has been rephrased, the result I was referring to was the results in Table 5.

Comment 7 (pg.15)

You have to section your samples away from this area of defects

Response

I believe the section on 'samples' should be categorised under sample defects. I included sub-section 4.1 with the heading ‘’Defects of Feedstock material and As-fabricated samples ’’ on page 15.

Comment 8 (pg.15)

I fail to see the relevance of this section, does it affect your results in any way. Please see comment above

Response

Section 4 of my manuscript uses the term 'Sample defects' to refer to all potential defects as mentioned in the first paragraph in section 4 that could have occurred during the fabrication process of my samples, regardless of whether they may impact the final results. This includes defects in the feedstock material within metallic powders, microstructural defects in the as-fabricated samples, spatter built-up on the lower layers, as well as surface morphology such as blobs and zits on the sample.

Comment 9 (pg.17)

Relevance? This looks more like a literature review with parts of an experimental procedure (Post-processing defects suppression strategies)

Response

Based on the comments of the reviewers, I agree with the reviewer therefore I have removed a section from the manuscript. The manuscript focuses on the analysis of the microstructure effect and properties of as-fabricated sample specimens. Hence, I did not analyse any post-processing experimental procedure or results to suppress defects. Possible further research will be done regarding post-processing defect suppression strategies in the near future.

Comment 10 (pg.17)

What does this mean ‘’machine specification’’

Response

The sentence has been revised and the term "machine specification" has been replaced with "selected process parameters".

In conclusion, we are pleased to inform you that we have made significant revisions to our manuscript in response to the reviewer's comments. We believe that these changes have greatly improved the quality and clarity of our work, bringing it in line with the standards and expectations of SAJIE. We are confident that our revised manuscript meets the requirements for publication and hope it will be approved for inclusion in your esteemed journal.

Thank you for your time and consideration

Kind Regards

Theo-Neal Booysen

On behalf of all authors.